CONF-961138--1

MODELING MICROSTRUCTURE DEVELOPMENT IN WELD METALS

S. A. David and S. S. Babu

Metals and Ceramic Division, Oak Ridge National Laboratory

Oak Ridge, TN 37831-6096, USA

ABSTRACT

Microstructure development in the weld metal region is controlled by various physical processes such as thermochemical reactions in liquid, solidification, and solid state transformations. There is a need for fundamental and generalized models that can predict the effect of these physical processes on microstructure development in a wide variety of alloy systems during welding processes. This paper describes certain advances made in the area of modeling the microstructure development in low–alloy steel, stainless steel, and Ni-base superalloy. In addition, this paper describes the importance of advanced analytical techniques for fundamental understanding of phase transformation mechanisms in welds.

Introduction

Integrated and generalized models, based on fundamental principles, for predicting microstructure development in both heat–affected zone (HAZ) and weld metal regions are necessary to develop a science-based tailoring of the composition, structure, and properties of welds. In addition, microstructure development in the weld metal region is the most complicated.[1] This complication arises because of various physical processes that occur in the arc plasma vapor state,[2,3] weld metal liquid state,[4,5] and solid state.[6–9] The outcome of each physical process that dominates at higher temperature influences the phase changes at lower temperature. For example, physical processes such as elemental transport in the weld metal, evaporation of alloying elements from the weld metal, and gas–metal reactions control the final weld metal composition. The weld metal composition, in turn, controls the microstructure development during solidification and solid state transformations. This type of sequential dependency of microstructure development in weld metals exists in almost all alloy systems. Various sophisticated models using analytical and numerical approaches exist for describing the elemental evaporation and dissolution of gases,[3] heat transfer and fluid flow,[10] solidification,[4] and solid state transformation in welds.[7,8] However, an integrated model that comprises all of the above processes is yet to be developed. Such an integrated model must also be capable of describing the microstructural degradation and changes during various postweld heat treatment schedules and service lives. This paper describes recent work on inclusion formation in low–alloy steel, advances in theoretical and physical modeling of solidification, and microstructure development in stainless steel and Ni-base superalloy welds. The importance of sophisticated analytical tools, such as atom-probe field-ion (APFIM), microscopy in modeling the phase transformations is also highlighted.

Inclusion Formation in Low-Alloy Steel Welds

A reaction that is known to influence microstructure development is inclusion formation. In steel welds, inclusions are oxides which are the result of a deoxidation reaction. In low–alloy steel weld metal, inclusions can improve the toughness by promoting the formation of a high–toughness ferritic phase known as acicular ferrite. The maximization of acicular ferrite leads to an optimum combination of strength and toughness.[11–15] A typical weld metal microstructure containing inclusions and acicular ferrite is shown in Fig. 1. The presence of oxide inclusions alone does not ensure the formation of acicular ferrite in steel welds. It is known that only certain kinds of inclusions aid in the nucleation of acicular ferrite;[7,11-13] the steel hardenability (chemical composition), austenite grain size (which is described in the next section), and welding conditions must also be conducive to form acicular ferrite in preference to other competing ferrite

morphologies.[16-18] Although certain inclusions aid in the formation of acicular ferrite, a very high volume fraction of inclusions may lead to poor properties. Therefore, it is necessary to control the inclusion characteristics to obtain the desired optimum microstructure.

The inclusion formation in a low–alloy steel weld is controlled by the concentrations of dissolved gases (such as oxygen and nitrogen) and deoxidizing elements (such as aluminum, titanium, silicon, and manganese). The dissolution of gases into the liquid steel is affected by the arc–atmosphere conditions around the molten steel.[19,20] The important inclusion characteristics are inclusion composition, size, and number density. The characteristics also include oxidation sequence and residual deoxidizing elements.[21-23] The residual deoxidizing elements in solid solution, such as Al, Ti, Si and Mn, that remain after the oxidation reaction control the transformation of austenite to ferrite at lower temperatures. Previous attempts[7,21,22] to predict inclusion composition assumed a fixed oxidation sequence of aluminum to Al_2O_3, titanium to Ti_2O_3, silicon to SiO_2, and manganese to MnO. This assumption was based on the ranking of the oxides Al_2O_3, Ti_2O_3 (or to other types of Ti_xO_y oxides), SiO_2, and MnO as per their standard free energy of formation. However, the oxidation sequence may change as a function of the concentration of reacting elements. Moreover, previous work did not model other inclusion parameters such as inclusion number density, size, and residual amounts of deoxidizing elements.

In this work, inclusion formation is described for a given nominal concentration of dissolved gases and deoxidizing elements. Inclusion formation will also be related to the rate at which the weld cools. The steps involved in the inclusion model include the calculation of (1) driving force for oxide formation, (2) homogeneous nucleation rates, (3) growth rates, and (4) overall oxidation kinetics as a function of temperature and composition. The methodologies for each of the above calculations are published elsewhere.[23] The isothermal oxidation kinetics calculations are then applied to the continuous cooling conditions.

Overall Oxidation Kinetics

The overall isothermal oxidation kinetics at a particular temperature T_1 involving a deoxidizing element (M) and oxygen (O) dissolved in liquid steel to produce an oxide inclusion of M_xO_y is given by the following equation:[23]

$$\zeta = 1 - \exp\left\{ - \left((8\pi/15) I_V \left(\alpha_3^*\right)^3 t^{\frac{5}{2}} / \Omega \right) \right\}, \qquad (1)$$

where ζ is the extent of reaction, I_v is the homogeneous nucleation rate of oxide M_XO_y per unit volume per second, α_3^* is the parabolic thickening rate of oxides in liquid steel, t is the time of reaction at temperature T_1, and Ω is the equilibrium volume fraction of M_XO_y at T_1, given by:

$$\Omega = \left(c_{\underline{M}}^{l} - c_{\underline{M}}^{il}\right) / \left(c_{\underline{M}}^{i} - c_{\underline{M}}^{il}\right) \tag{2}$$

where $c_{\underline{M}}^{l}$ is the average concentration of the deoxidizing element, $c_{\underline{M}}^{il}$ is the concentration of deoxidizing element in the liquid in equilibrium with the inclusion, and $c_{\underline{M}}^{i}$ is the concentration of deoxidizing element in the inclusion in equilibrium with the liquid. The equilibrium concentration of deoxidizing element, $c_{\underline{M}}^{il}$, is obtained by the construction of a tie line to the deoxidation phase diagram[23] (the concentrations are in mole fraction). The expressions for calculating other terms α_3^* and I_v are given elsewhere.[23] Equation (1) enables one to predict the isothermal oxidation kinetics for various oxides as a function of nominal composition and temperature. Isothermal oxidation kinetics calculations were applied to two weld metal compositions (SW1: Fe-0.07C-0.8Si-1.7Mn-0.025Ti-0.026Al-0.084O wt % and SW2: Fe-0.07C-0.3Si-1.7Mn-0.003Ti-0.017Al-0.024O wt %), and the time–temperature–transformation (TTT) diagrams for ζ = 0.1 were calculated as a function of temperature. The comparisons are shown in Fig. 2. The difference in weld metal deposit chemistry changed the oxidation sequence as a function of decreasing temperature from 2300 K. Isothermal oxidation kinetics calculations were applied to continuous cooling conditions. The integrated number density of the first forming oxide was taken as the final number density of inclusions in the steel weld (this assumption is based on the observation of heterogeneous and layered inclusion structures).[21] The final inclusion number density is given by:

$$Number\ Density = \sum_{i=T_{start}}^{i=T_{end}} I_V^{oxide1} \times \Delta t_i \tag{3}$$

where I_V^{oxide1} is the nucleation rate of the first forming oxide as a function of temperature, and Δt_i is the time spent at each temperature from T_{start}, the temperature at which the first oxide starts to form, to T_{end}, the temperature at which the extent of reaction, ζ, of the first oxide reaches 0.9. The accumulated volume fraction of oxide inclusions at the liquidus temperature was taken as the

final volume fraction of oxides, and the residual liquid composition at 1800 K was related to the amount of deoxidizing elements in solid solution. With the knowledge of the final inclusion volume fraction (V_f) and final number density, the average inclusion radius was calculated.

Inclusion Model Validation

The inclusion model developed in this work was validated with experimental results. The cooling rate data necessary for the calculation of inclusion characteristics were obtained by using the equation given by Ion et al.[24] However, it is important to note that these cooling rate calculations are approximate, and, ideally, one should use the weld metal cooling rate calculations which consider the heat flow and mass transfer in the weld-pool region.[25] The calculations were validated with the experimental data of Kluken and Grong.[21, 26] A comparison of experimental results of inclusion composition and final number density published by Kluken and Grong[21, 26] with the calculations of the present inclusion model is shown in Fig. 3. The comparison shows that the present inclusion model predicts a trend similar to that of the experimental data. However, the predictions are not exact. The comparison of experimental measurement and theoretical estimation of aluminum in solid solution showed a fair correlation.[27-29] However, excellent agreement is observed with the predicted titanium levels in solid solution. The inaccuracies of the inclusion model in predicting inclusion characteristics is attributed to the fluid flow effects on heat transfer[25] and inclusion formation and the formation of complex oxides, sulfides, and nitrides during the final stages of oxidation and solidification. Further work is in progress to remove the above limitations in the present inclusion model.[27-29]

Weld Solidification

Weld solidification controls grain structure, segregation, defects[5] and inclusion distribution.[30] Although there are some similarities between ingot or casting solidification and weld–pool solidification, modeling of the solidification in the weld metal region is evolving. In this section, various attempts at modeling the weld solidification by extending the current knowledge of the freezing of single crystals, castings, and ingots is described. In addition, recent work on rapid solidification effects in the weld metal is discussed. Modeling of weld or ingot solidification is associated with the nucleation and growth of a solid phase from the liquid. Generalized weld solidification models, in addition to describing nucleation and growth, must be capable of describing solute distribution, grain structure development, and rapid solidification effects.[1,4,31,32] A basic understanding of these concepts is necessary to develop an integrated model capable of describing solidification in a wide variety of welding process conditions and alloy systems.

During welding, weld-pool solidification proceeds from the pre–existing solid substrate without any nucleation barrier. In the case of autogeneous welding, solidification occurs spontaneously by epitaxial growth. In cases where filler metal is used, epitaxial growth may still occur. In addition to heterogeneous nucleation on the solid base material, inoculants have been successfully used to promote nucleation.[33] Other methods to promote nucleation in the weld-pool include weld-pool stirring and arc oscillations.[5] Although the mechanisms of nucleation in weld metal are well understood, not much attention is given to modeling this phenomenon. Often, weld solidification models assume the epitaxial growth in their models, and for most of the cases, the assumption seems to be appropriate. However, to describe the effect of inoculants, arc oscillations, and weld–pool stirring, heat and mass transfer models[28,10] have to be coupled with either probabilistic models, such as cellular automata (CA),[34-36] or deterministic models using the fundamental equations of nucleation as described earlier.[23]

The development of microstructural features during the growth of solid in the weld metal region is controlled by the shape of the solid/liquid interface and its stability. Theories for interface stability under conditions of equilibrium at the interface for normal solidification, or under extreme nonequilibrium conditions prevalent during rapid solidification, have been developed.[37,38] These theories can be extended to weld–pool solidification. The parameters that determine the solidification microstructure in castings are growth rate (R_s), temperature gradient (G), undercooling (ΔT_u), and alloy composition. It is well known that the temperature gradient and growth rate are important in the combined forms GR_s (cooling rate) and G/R_s since they influence the scale of the solidification substructure and the solidification morphology, respectively. In welding, where molten pool is translated through the material, both G and GR_s vary considerably across the weld-pool region. Figure 4 shows schematically the influence of G and R on the microstructural variations within the weld metal. The figure shows the regions of planar to cellular transition (PCT) and cellular to equiaxed transition (CET). An example of the transition from planar to cellular–type solidification microstructure is shown in Fig. 5.

The method of using GR_s and G/R_s relations to depict the solidification morphology is proved to be simple and elegant. However, modeling of solidification morphology in a typical weld must consider other factors such as the fluid flow, the density of grains at the fusion line taking part in the epitaxial growth, the effect of base plate texture on the growth patterns in the weld metal region,[36,39] and the amount of total undercooling (ΔT). Although the CA models[35] can be used for modeling the spatial morphology and transitions from cellular to equiaxed solidification in casting processes, much work needs to be done in improving the extension of this method to welds.[36] Future solidification morphology models, such as CA techniques,[34-36] should consider solute diffusion and CA models should be coupled with the numerical models that consider the diffusion of partitioned alloying elements between solid and liquid phases.[40,41]

Solute distribution during weld-pool solidification is an important phenomenon resulting in segregation that can significantly affect weldability, microstructure, and properties. Various studies on extending different solidification models to describe solute distribution are summarized.[5] In describing the solute distribution under dendritic growth conditions, consideration should be given to redistribution at the dendrite tip and in the interdendritic regions. The solute distribution at the dendrite tip is determined, to a larger extent, by the dendrite tip undercooling, which is made up of four components: thermal undercooling, kinetic undercooling, constitutional undercooling, and undercooling due to tip curvature.[5]

In welding, the first two contributions can be ignored. However, since the microstructures are much finer in scale in welds than in castings, the contribution to the total tip undercooling due to the curvature effect is very significant.[5] The effect of increased undercooling at the dendrite tip would be to solidify at a composition closer to the overall composition and thus reduce the extent of microsegregation. Dendrite tip undercoolings in welds have been estimated by measuring dendrite core compositions in two different alloy systems, Al–Cu and Fe–Nb, after gas tungsten arc welding.[59] The estimated dendrite tip undercooling has been found to be significant. Considering the solute redistribution in the interdendritic regions, it may be sufficient to extend the solidification model for microsegregation in castings to welds. In such cases, the weld solidification models can assume little or no diffusion in the solid while complete mixing of solutes in the liquid by convection. This can be achieved by the Scheil equation[42] or modified Scheil equations that consider the diffusion[40,41] in the solid during welding.

During welding, the growth of solid often occurs by epitaxial growth from the partially melted grains in the base metal. Therefore, the weld metal grain structure is predominantly determined by the base metal grain structure and the welding conditions. In addition, crystallographic growth competitions will influence the grain structure development. It is well known that grain growth into the liquid region is favored along easy growth crystallographic directions, for example <100> in cubic metals. Conditions for growth are optimum when one of the easy growth directions coincides with the heat flow direction. Since the solid/liquid interface is essentially perpendicular to the heat flow direction, the pool shape influences the optimum growth direction. Using a recently developed geometrical analysis and expressing the solidification front normal and the crystallographic growth directions in terms of a fixed set of reference axes, dendrite growth selection process in Fe–Ni-Cr single-crystal welds can be evaluated.[43-46] This analysis can also be extended for the grain growth selection process. These types of geometrical models can also be used to describe the three-dimensional reconstruction of the weld-pool shape.

With the increased use of high–energy beam processes, such as electron and laser beams for welding, observations of nonequilibrium microstructures under rapid cooling conditions are

becoming common. Such observations are well documented for austenitic stainless steel welds. [46-51] Figure 6 shows a fully austenitic stainless steel weld microstructure in a laser weld, which would normally contain a duplex austenite plus ferrite microstructure. This microstructure is attributed to a change in the mode of freezing from primary ferrite (δ) to primary austenite during rapid solidification. Modeling of this kind of transition in rapid solidification is just evolving. In rapid cooling conditions, a significant departure from local equilibrium at solid/liquid interface may occur. As a result, nonequilibrium structure and, in some cases, partitionless solidification can be observed. The magnitude of these departures is not fully understood and characterized. Another consequence of rapid solidification effect is that plane front solidification may become stable at extreme rapid growth rates.[5,52]

SOLID STATE TRANSFORMATIONS

In general, inclusion formation and solidification are part of the phase transformations that occur in any weld metal microstructure development. However, in some alloys, the solid state transformations that occur in the weld metal region control the final microstructure and properties. Therefore, modeling solid state transformations in welds is important in developing generalized, integrated models for weld metal microstructure development. Various solid state transformations that occur in welds during welding and in service can be grouped into four categories as follows: (1) phase changes involving diffusional processes such as precipitation or dissolution of the second phase in the matrix; (2) solid state processes involving grain growth, coarsening, and solute redistribution; (3) phase changes involving displacive transformations such as martensitic transformations; and (4) phase changes such as spinodal decomposition. Moreover, it is important to note that some of the above phase changes may occur concurrently and interact with each other. Therefore, a prior knowledge of various phase transformations that occur in an alloy system is necessary before developing a model for weld metal microstructure development. Various aspects of modeling solid state transformation are published elsewhere.[7] In this section, two examples to describe the importance of experimental high-resolution analysis of microstructure as an aid to model solid state phase transformations in welds are presented.

Analysis of residual element segregation in stainless steel welds

Type 308 stainless steel welds with the addition of 0.007 wt % boron showed improved creep properties.[54] Since boron additions may improve the properties by altering the microstructure, attempts were made to relate the microstructures that develop during welding.[54] The microstructural development during welding was found to be similar in welds with and without boron addition.[54] Therefore, it is important to study the boron redistribution between phases during weld metal cooling. The equilibrium solidification and partitioning in boron containing

welds were simulated using ThermoCalc™ software[55] and the Scheil method.[42] Since the solubility levels of boron in ferrite and austenite are small, as the solidification proceeds, the remaining liquid becomes enriched in boron. According to thermodynamic calculations, the boron concentration at the ferrite–austenite interface is likely to be on the order of 1 at. % B. This prediction can be validated using APFIM. APFIM analysis was performed on a boron-containing weld in the as–welded state. A field ion micrograph of an austenite–ferrite interface is shown in Fig. 7(*a*). The interface was decorated by a series of brightly imaging atoms indicative of solute segregation. An atom probe composition profile measured across an austenite–ferrite boundary is shown in Fig. 7(*b*). The maximum boron concentration at the interface was found to be ~ 2 at. % which compares well with thermodynamic calculations.[56]

Ni-base superalloy weld microstructure development

It has long been recognized that welding of Ni-base single-crystal superalloy will play a vital role in repair welding of land–based gas turbine components. As a result, modeling and characterization of microstructure development in Ni-base superalloy welds has gained importance.[57] Babu et al.[57] studied the microstructure development in an electron-beam-welded PWA–1480 single–crystal superalloy. A low-magnification transmission electron micrograph [see Fig. 8(*a*)] shows a boundary between two dendrite arms. Along the interdendritic regions, large γ' precipitates interlaced by thin films of γ phase were observed. The morphology of these large γ' precipitates with penetrated γ phase suggests that these γ' precipitates formed during the final stages of solidification through eutectic reaction, $L \rightarrow \gamma + \gamma'$. Within the core of the dendrite, fine, cuboidal $L1_2$–ordered γ' precipitates were observed. The above microstructural development can be explained with the help of a quasi-binary diagram of the Ni-Al-Cr alloy system, as shown in Fig. 8(*b*).

To illustrate the microstructural development in the PWA-1480 alloy, the phase changes in the Ni–11.0 at. % Al–11.5 at. % Cr alloy, as it solidifies from the liquid state, are discussed below. According to the equilibrium phase diagram, the solidification to γ starts at ~ 1698 K and is completed at ~ 1685 K. Since the weld cooling conditions are far from equilibrium conditions, this may not be an actual representation of the weld solidification. The variations in the compositions of the γ matrix and liquid phase during such a solidification in a Ni–11.0 at. % Al–11.5 at. % Cr alloy (assuming Scheil's model) were calculated using the ThermoCalc™ software.[55] The calculations indicate that the solidus temperature is lowered by 50 K, i.e., to 1635 K. ThermoCalc™ calculations also suggested that the final liquid, due to solute enrichment, will undergo a eutectic reaction at ~ 1630 K as shown in Fig. 8(*b*). The observation [see Fig. 8(*a*)] of large γ' precipitates interlaced with films of the γ phase supports this mode of solidification for the weld. However, this work[57] is not strictly valid, since Ti, Ta, W, and Co

will modify the partitioning characteristics between the γ and γ' phases. Therefore, one has to use other calculation methods.[58] Further work is necessary to extend the thermodynamic calculations with consideration of other elements to predict the partitioning characteristics of γ and γ' phases during continuous cooling and thermal aging conditions.

SUMMARY

This paper describes state-of-the-art technology of modeling of various physical processes that occur within the weld metal region as the weld-pool starts to cool. In particular, it addresses inclusion formation, solidification, and solid state transformation. Models to describe these events are still evolving. The results indicate that it should be possible to develop an integrated model for the prediction of weld metal microstructure.

ACKNOWLEDGMENTS

The authors thank Drs. A. N. Gubbi and A. J. Duncan for their helpful comments, Dr. K. Mundra and Prof. T. DebRoy of The Pennsylvania State University for collaborative work on heat transfer and fluid flow in welds, and K. Spence for editing. Research was sponsored by the Division of Materials Sciences, U.S. Department of Energy, under contract DE-AC05-96OR22464 with Lockheed Martin Energy Research Corporation.

REFERENCES

1. T. DebRoy and S. A. David: *Rev. Mod. Phys.*, 1995, **67**, 85–112.
2. J. Szekely: *Advances in Welding Science and Technology*, S. A. David, Ed. ASM, Materials Park, Ohio, 1986, 3–14.
3. T. DebRoy: *Mathematical Modeling of Weld Phenomena*, H. Cerjak and K. E. Easterling, Ed., The Institute of Materials, London, 1993, 24–38.
4. S. A. David and J. M. Vitek: *Mathematical Modeling of Weld Phenomena*, H. Cerjak and K. E. Easterling, Ed., The Institute of Materials, London, 1993, 41–59.
5. S. A. David and J. M. Vitek: *Int. Mater. Rev.*, 1989, **34**, 213–245.
6. D. L. Olson, S. Liu, and G. R. Edwards: *Mathematical Modeling of Weld Phenomena*, H. Cerjak and K. E. Easterling, Ed. The Institute of Materials, London, 1993, 89–108.
7. H. K. D. H. Bhadeshia and L.–E. Svensson: *Mathematical Modeling of Weld Phenomena*, H. Cerjak and K. E. Easterling, Ed., The Institute of Materials, London, 1993, 109–180.
8. K. E. Easterling: *Mathematical Modeling of Weld Phenomena*, H. Cerjak and K. E. Easterling, Ed., The Institute of Materials, London, 1993, 183–200.

9. B. Buchmayr: *Mathematical Modeling of Weld Phenomena*, H. Cerjak and K. E. Easterling, Ed., The Institute of Materials, London, 1993, 227–240.
10. T. Zacharia and S. A. David: *Mathematical Modeling of Weld Phenomena*, H. Cerjak and K. E. Easterling, Ed., The Institute of Materials, London, 1993, 3–23.
11. Ø. Grong and D. K. Matlock: *Int. Met. Rev.*, 1986, **31**, 27-48.
12. D. J. Abson: *Welding Institute Report 69/1978*, The Welding Institute, Abington, United Kingdom, 1980, 1-11.
13. D. J. Abson: *Weld. World*, 1989, **27**, 76-101.
14. Y. Ito and M. Nakanishi: *Sumitomo Search*, 1976, **15**, 42-62.
15. S. Liu, and D. L. Olson: *Weld. J.*, 1986, **65**, 139s-149s.
16. P. L. Harrison and R. A. Farrar: *J. Mater. Sci.*, 1981, **16**, 2218–2226.
17. J. R. Yang and H. K. D. H. Bhadeshia: *Advances in Welding Science and Technology*, S. A. David, Ed., ASM, Materials Park, Ohio, 1986, 209–213
18. S. S. Babu and H. K. D. H. Bhadeshia: *Mater. Sci. Technol.*, 1990, **6**, 1005-1020.
19. S. A. David, T. DebRoy, and J. M. Vitek: *MRS Bull.*, 1994, **XIX**, 29-35.
20. S. A. David and T. DebRoy: *Science*, 1994, **257**, 497-502.
21. A. Kluken and Ø. Grong: *Metall. Trans. A*, 1989, **20A**, 1335–1349.
22. F–C. Liao and S. Liu: *Weld. J.*, 1992, **71**, 94s-103s.
23. S. S. Babu, S. A. David, J. M. Vitek, K. Mundra, and T. DebRoy: *Mater. Sci. Technol.*, 1995, **11**, 186-199.
24. J. C. Ion, K. E. Easterling, and M. F. Ashby: *Acta Metall.*, 1984, **32**, 1949-1962.
25. K. Mundra, T. DebRoy, S. S. Babu, and S. A. David: submitted for publication in *Weld. J.*, 1995.
26. A. Kluken: "Modeling of reaction sequence during deoxidation and solidification of steel weld metals," Ph.D. thesis, University of Trondheim, Norway, 1990.
27. S. S. Babu, S. A. David, J. M. Vitek, K. Mundra, and T. DebRoy: *Trends in Welding Research*, Gatlinburg, Tennessee, June 5–8, 1995.
28. K. Mundra, T. DebRoy, S. S. Babu, and S. A. David: *Trends in Welding Research*, Gatlinburg, Tennessee, June 5–8, 1995.
29. S. S. Babu and S. A. David: Unpublished work, Oak Ridge National Laboratory, Oak Ridge, Tennessee, 1995.
30. A. A. B. Sugden and H. K. D. H. Bhadeshia: *Metall. Trans. A*, 1988, **19A**, 669–674.
31. S. A. David, J. M. Vitek, T. Zacharia, and T. DebRoy: Proceedings of *Physical Aspects of Arc Welding*, September 1, 1993, International Institute of Welding,, Glasgow, United Kingdom, 95–112.

32. S. A. David, J. M. Vitek, S. S. Babu, and T. DebRoy: Proceedings of *42nd National Welding Conference*, Vol. 2., Welding Technology Institute of Australia, Silverwater, New South Wales, Australia, 1994.
33. J. C. Villafuerte, H. W. Kerr, and S. A. David: *Mater. Sci. Eng.*, 1995, **A194**, 187–191.
34. M. Rappaz and Ch.–A. Gandin, *Acta Metall. Mater.*, 1993, **41**, 345–360.
35. Ch.–A. Gandin, M. Rappaz, and R. Tintillier: *Metall. Trans. A.*, 1993, **24A**, 467–479.
36. W. B. Dress, T. Zacharia, and B. Radhakrishnan: *Modeling and Control of Joining Processes*, T. Zacharia, Ed., American Welding Society, Miami, Florida, 1994, 321–328.
37. W. Kurz and D. J. Fisher: *Fundamentals of Solidification*, Trans Tech., Aedermannsdorf, Switzerland, 1989.
38. M. C. Flemings: *Solidification Processing*, McGraw-Hill, New York, 1974.
39. S. S. Babu, H. K. D. H. Bhadeshia, and L.–E. Svensson: *J. Mater. Sci. Lett.*, **10**, 1991, 142-144.
40. J. A. Brooks and M. I. Baskes: *Advances in Welding Science and Technology*, S. A. David, Ed., ASM, Materials Park, Ohio, 1986, 93–99.
41. T. Matsumiya, T. Koseki, W. Yamada, and Y. Ueshima: *Nippon Steel Technical Report*, 1993, **57**, 50–56.
42. E. Scheil: *Z. Metall.*, 1942, **34**, 70.
43. M. Rappaz, S. A. David, J. M. Vitek, and L. A. Boatner: *Metall. Trans, A.*, 1989, **20A**, 1125–1138.
44. M. Rappaz, S. A. David, J. M. Vitek, and L. A. Boatner: *Metall. Trans. A.*, 1990, **21A**, 1767–1782.
45. S. A. David, J. M. Vitek, M. Rappaz, and L. A. Boatner: *Metall. Trans, A.*, 1990, **21A**, 1753–1766.
46 M. Rappaz, S. A. David, J. M. Vitek, and L. A. Boatner: *Metall. Trans, A.*, 1993, **24A**, 1433–1446.
47. S. A. David and J. M. Vitek: *Lasers in Metallurgy*, K. Mukerjee and J. Mazumder, Ed., TMS, Warrendale, Pa., 1981, 2247–2254.
48. J. M. Vitek, A. DasGupta, and S. A. David: *Metall. Trans. A.*, 1983, **14A**, 1833-1841.
49. S. A. David, J. M. Vitek, and T. L. Hebble: *Weld. J.*, 1987, **66**, 289s.
50. S. Katayama and A. Matsunawa: *Proc. ICALEO*, 1984, 60–67.
51. J. W. Elmer, S. M. Allen, and T. W. Eagar, *Metall. Trans. A*, 1989, **20A**, 2117–2131.
52. W. Kurz: *Fourth International Conference on Trends in Welding Research*, Gatlinburg, Tennessee, June 5–8, 1995.

53. S. A. David and S. S. Babu: "Microstructure modeling in weld metal," in Proceedings of an *International Conference on Numerical Analysis of Weldability*, Graz-Saggau, Austria, September 25-27, 1995.
54. S. S. Babu, S. A. David, J. M. Vitek, and M. K. Miller: *Appl. Surf. Sci.*, 1995, **87/88**, 207–215.
55. B. Sundman, B. Jansson, and J.–O. Andersson: *Calphad,* 1985, **9**, 153-190.
56. S. S. Babu, S. A. David, J. M. Vitek, and M. K. Miller: *Metall. Mater. Trans. A,* 1996, **27A**, 763-774.
57. S. S. Babu, S. A. David, and M. K. Miller: *Appl. Surf. Sci.*, **94/95**, 1996, 280-287.
58. M. Enomoto, H. Harada, and M. Yamazaki: *Calphad*, 1991, **15**, 143.

Figure Captions

Fig. 1 Typical weld metal microstructure observed in a low-alloy steel weld.

Fig. 2 A comparison of the transformation time (for fraction transformed, $\zeta = 0.1$) for various oxides as a function of temperature for two steel compositions: (*a*) SW1: Fe-0.07C-0.8Si-1.7Mn-0.025Ti-0.026Al-0.084O wt. % and (*b*) SW2: Fe-0.07C-0.3Si-1.7Mn-0.003Ti-0.017Al-0.024O wt. %.

Fig. 3 Comparison of experimental inclusion characteristics measured by Kluken and Grong[21] and the calculated inclusion characteristics by the present inclusion model: (*a*) inclusion composition and (*b*) inclusion number density.

Fig. 4 (*a*) Schematic illustration of weld microstructure across the fusion zone and (*b*) corresponding schematic variation of G, R, GR and G/R values as a function of position.

Fig. 5 Optical micrograph of stainless steel weld metal region and heat-affected zone. The micrograph clearly shows the fusion line, with planar growth; the region of transition from planar to cellular growth; and the region of cellular growth.

Fig. 6 Duplex (austenitic plus ferritic) structure in conventional weld overlay and fully austenitic structure obtained by autogeneous laser weld on the same overlay.

Fig. 7 (*a*) Field ion micrograph of the as-welded sample showing (δ) ferrite–austenite boundary and (*b*) composition profile indicating the presence of boron along the (δ) ferrite–austenite boundary.

Fig. 8 (*a*) Transmission electron micrograph of the PWA-1480 weld metal region in the as-welded condition showing two dendritic grains, dendritic boundary, and eutectic γ' precipitate (marked by an arrow) along the dendritic boundary. The electron diffraction pattern (inset), taken near to the $[001]_\gamma$ zone, shows the superlattice reflections from γ' precipitates. (*b*) A quasi-binary diagram of the Ni-Al-Cr system with 11.5 at. % Cr calculated by ThermoCalc™ software.[25] The dotted line shows the composition corresponding to 11.0 at. % Al. In this phase diagram, the tie lines are not in the plane of the diagram.

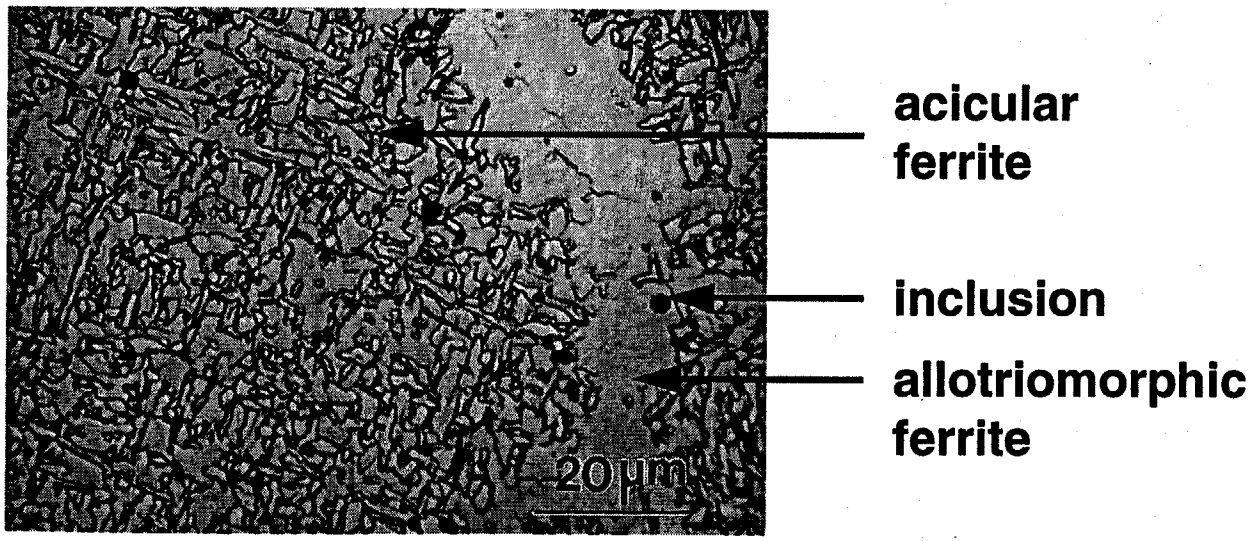
acicular
ferrite
inclusion
allotriomorphic
ferrite
20 μm

Fig. 1

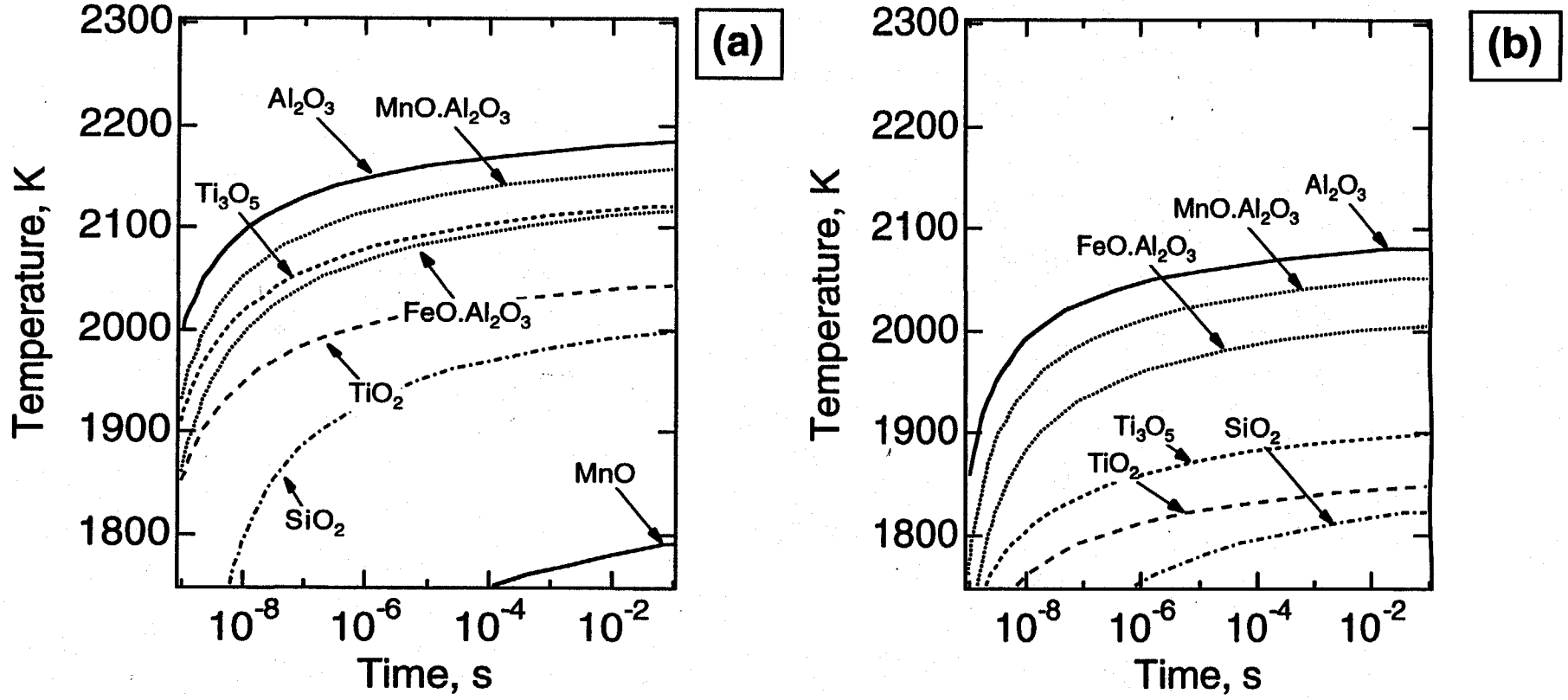
(a)
2300
2200
2100
2000
1900
1800
Temperature, K
Al_2O_3
$MnO.Al_2O_3$
Ti_3O_5
$FeO.Al_2O_3$
TiO_2
MnO
SiO_2
10^{-8}
10^{-6}
10^{-4}
10^{-2}
Time, s
(b)
2300
2200
2100
2000
1900
1800
Temperature, K
Al_2O_3
$MnO.Al_2O_3$
$FeO.Al_2O_3$
Ti_3O_5
SiO_2
TiO_2
10^{-8}
10^{-6}
10^{-4}
10^{-2}
Time, s

Fig. 2

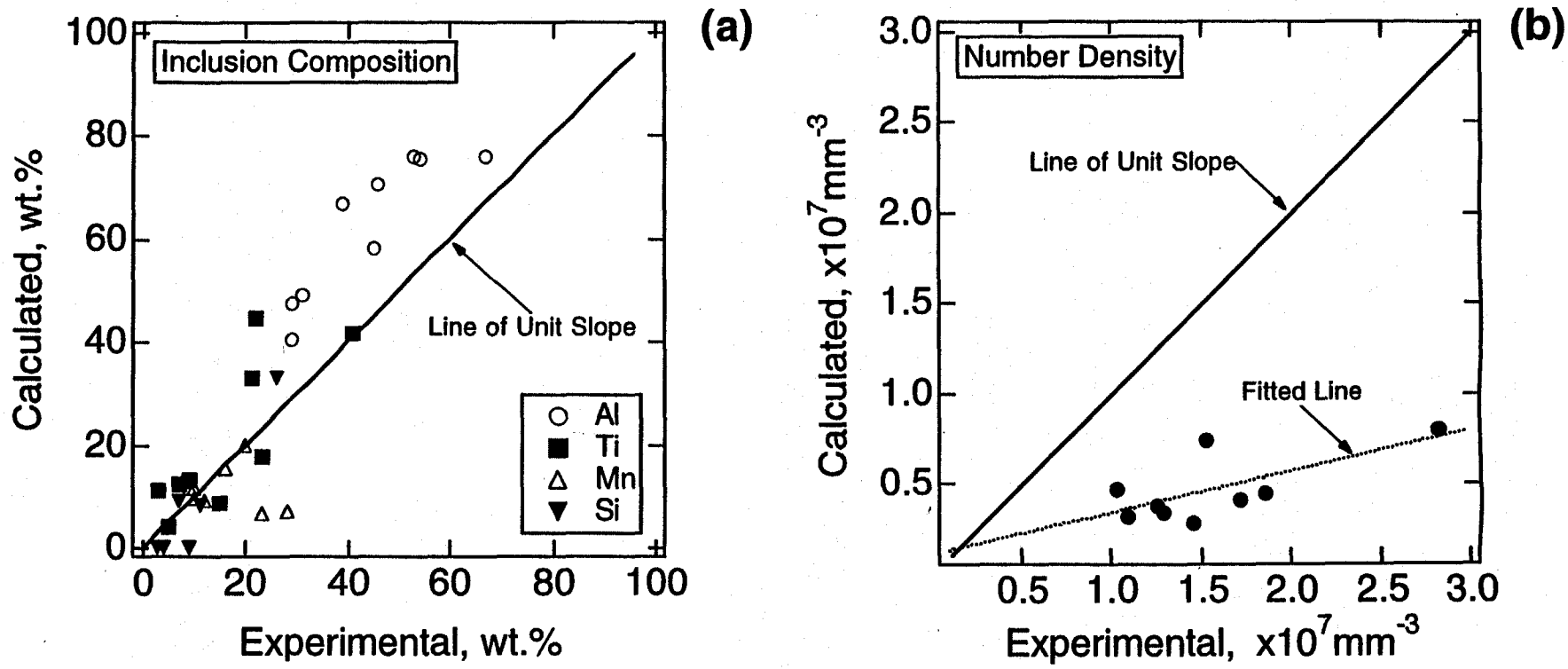
(a)
Inclusion Composition
Calculated, wt.%
Experimental, wt.%
Line of Unit Slope
Al
Ti
Mn
Si
0
20
40
60
80
100
(b)
Number Density
Calculated, x10^7mm^-3
Experimental, x10^7mm^-3
Line of Unit Slope
Fitted Line
0.5
1.0
1.5
2.0
2.5
3.0

Fig. 3

FIG.4

FIG.4

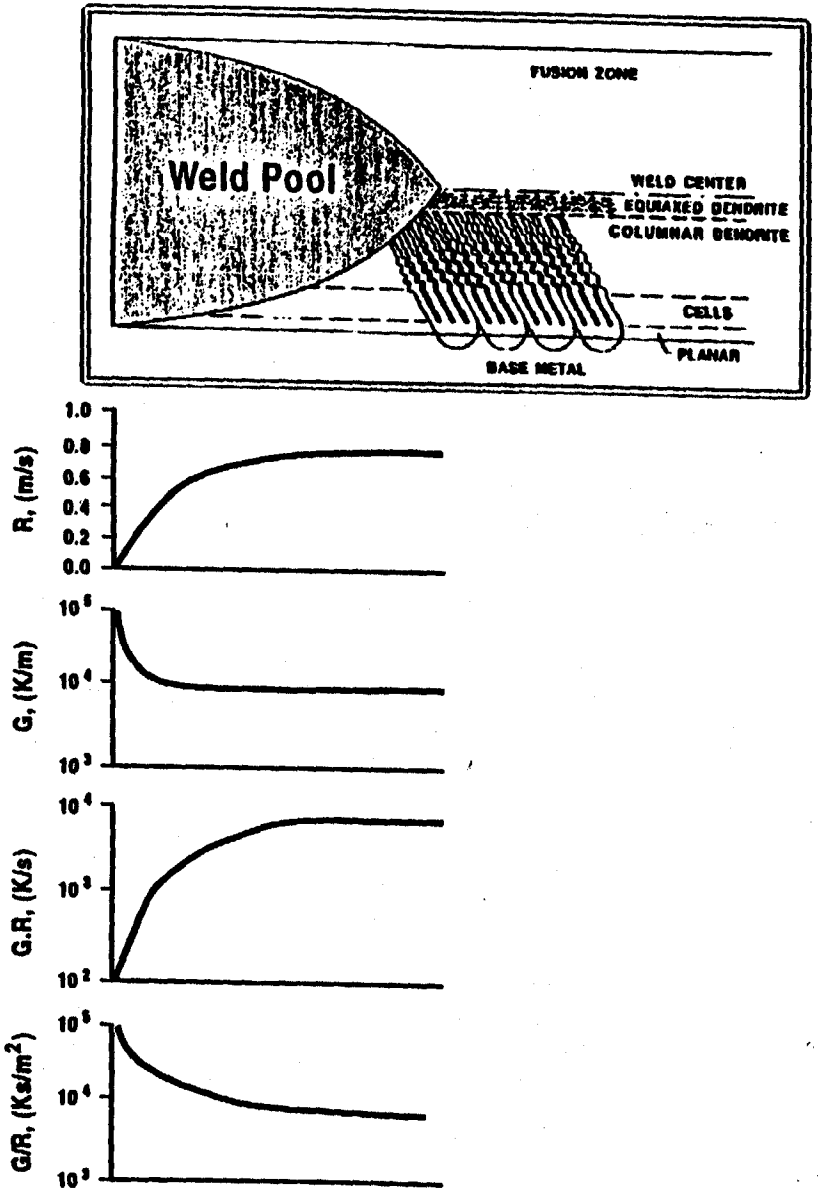
(a)
FUSION ZONE
Weld Pool
WELD CENTER
EQUIAXED DENDRITE
COLUMNAR DENDRITE
CELLS
PLANAR
BASE METAL
(b)
R, (m/s)
1.0
0.8
0.6
0.4
0.2
0.0
G, (K/m)
10^5
10^4
10^3
G.R, (K/s)
10^4
10^3
10^2
G/R, (Ks/m^2)
10^5
10^4
10^3

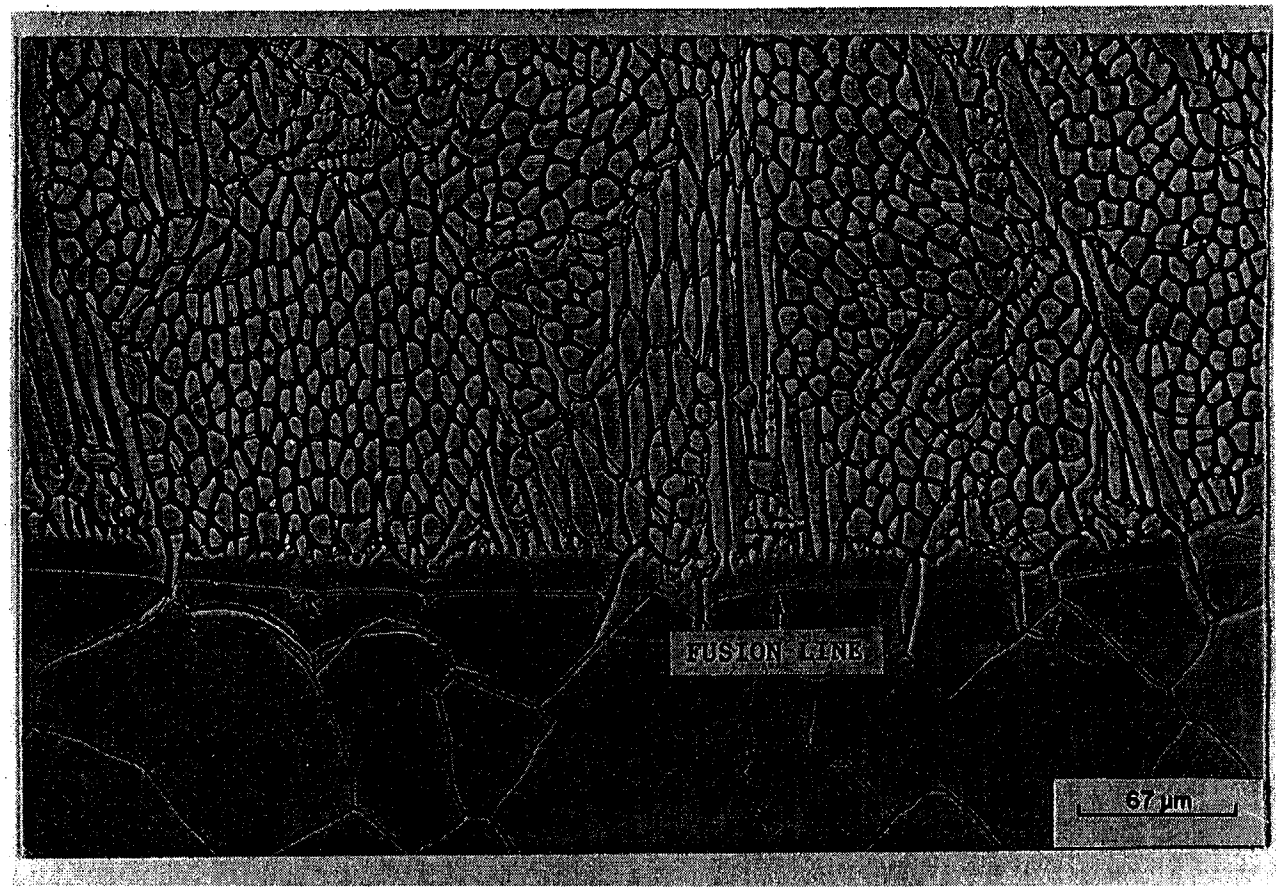

Fig. 5

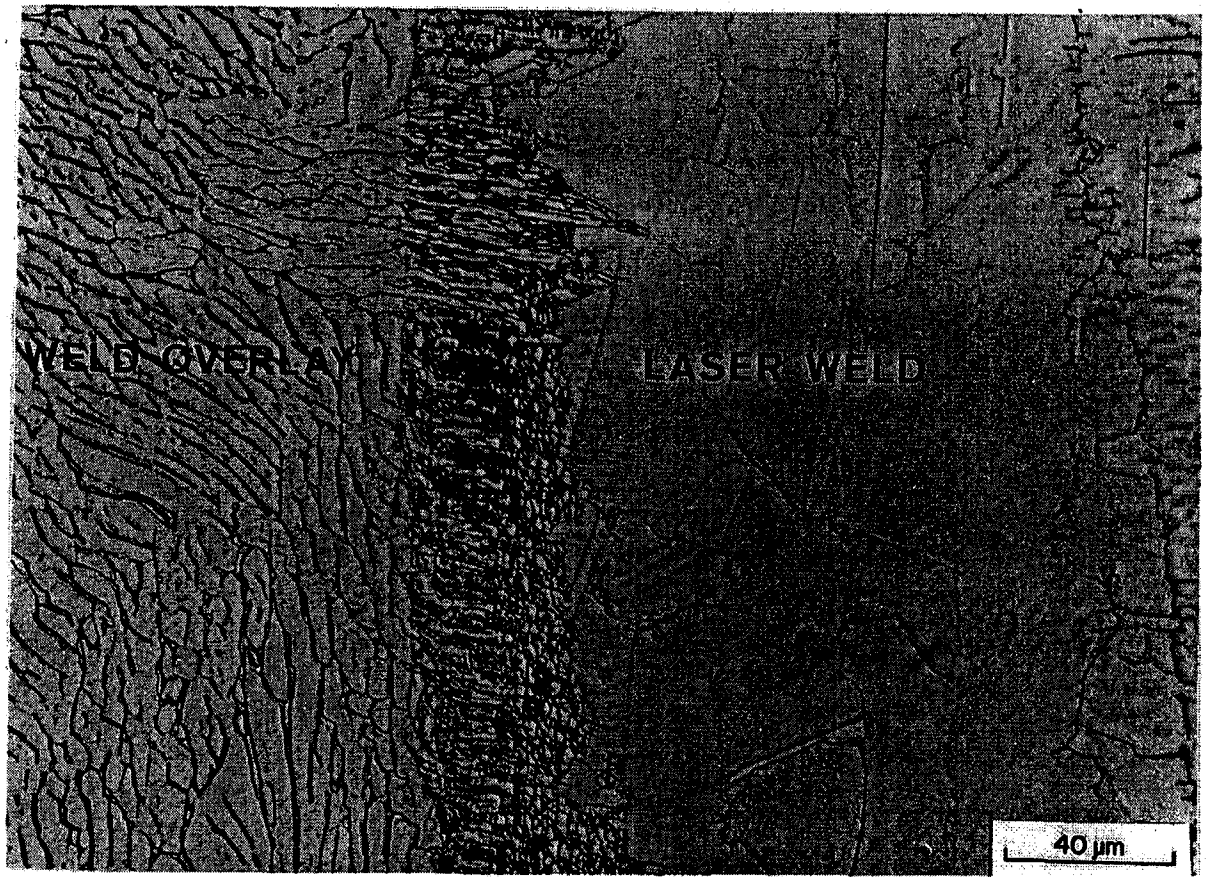

Fig. 6

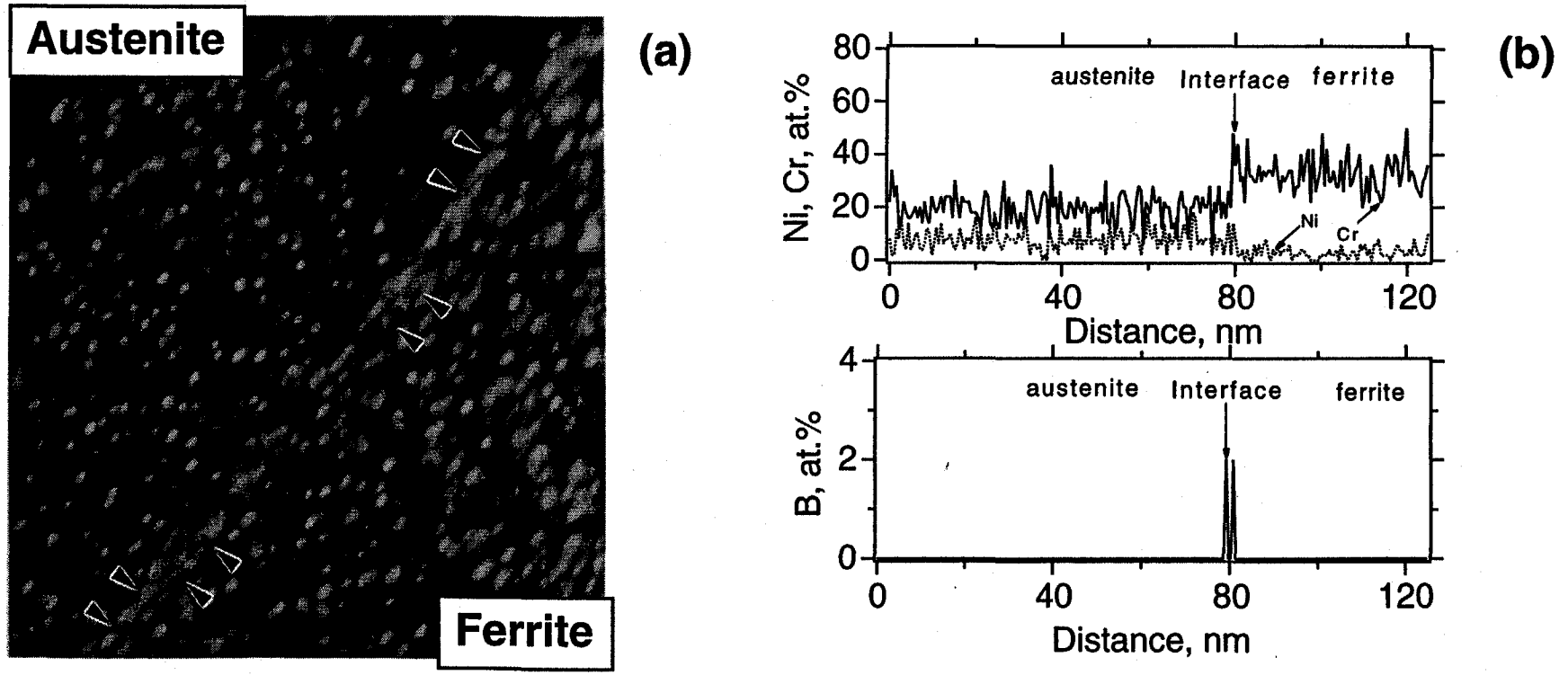
Austenite
Ferrite
(a)
(b)
austenite
Interface
ferrite
Ni, Cr, at.%
Ni
Cr
Distance, nm
B, at.%
Distance, nm

Fig. 7

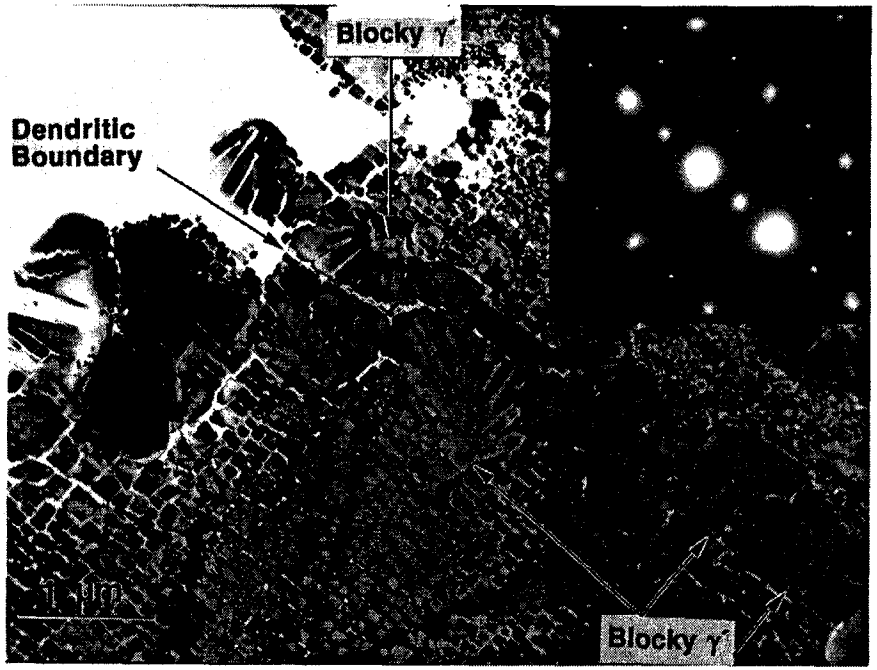
Blocky γ
Dendritic Boundary
1 μm
Blocky γ'

(a)

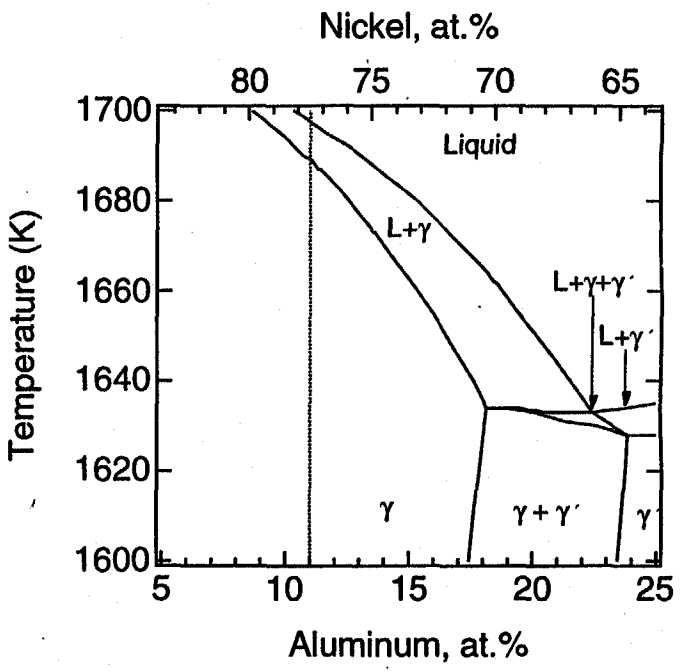
Nickel, at.%
80
75
70
65
1700
1680
1660
1640
1620
1600
Temperature (K)
Liquid
L+γ
L+γ+γ'
L+γ'
γ
γ + γ'
γ'
5
10
15
20
25
Aluminum, at.%

(b)

Fig. 8